Arabian Journal of Chemistry (2020) **13**, 1323–1334

King Saud University

Arabian Journal of Chemistry

www.ksu.edu.sa
www.sciencedirect.com

ORIGINAL ARTICLE

Layered magnetite nanoparticles modification – synthesis, structure, and magnetic characterization

U. Klekotka [a], D. Satula [b], P. Nordblad [c], B. Kalska-Szostko [a],*

[a] *University of Bialystok, Institute of Chemistry, Ciolkowskiego 1K, 15-245 Bialystok, Poland*
[b] *University of Białystok, Faculty of Physics, Ciolkowskiego 1L, 15-245 Bialystok, Poland*
[c] *Uppsala University, Ångström Laboratory, Lägerhyddsvägen 1, Uppsala, Sweden*

Received 11 August 2017; accepted 1 November 2017
Available online 9 November 2017

KEYWORDS

Magnetic materials;
Nanoparticles;
Structural characterization;
Magnetic characterization

Abstract Core-shell and multilayered nanoparticles based on magnetite core with different metallic spacing and over-layers are prepared in one pot synthesis and characterized. The spacer layers were made from Au, Cu or Ag precursors. The nanoparticles were fabricated by a modified chemical seed based method. The obtained nanoparticles were examined by X-ray diffraction, Energy-dispersive X-ray spectroscopy, Transmission Electron Microscopy, Differential Scanning Calorimetry and Infra-red spectroscopy. Magnetic properties of the nanoparticles were tested by Mössbauer spectroscopy and Magnetometry. Magnetization and Mössbauer measurements show that the presence of the metallic layers influences the magnetic state of the particles. XRD and EDX confirm layered structures of nanoparticles. Proposed synthesis allows for fabrication of layered particles with controlled morphology and register properties changes which are related to the nature of each subsequent layer.

1. Introduction

Superparamagnetic nanoparticles have become intensively investigated in recent years because of their unusual electrical, optical, magnetic, and mechanical properties (Ahadpour Shal and Jafari, 2014; Vatta et al., 2006; Zhu et al., 2003). The extraordinary properties of these materials allow the use of magnetic nanoparticles in new bio-medical applications such as drug delivery, cell separation, bio-separation or enrichment means in the biomedical utility (Angelakeris et al., 2015; Xiong et al., 2013; Lingyan Wang et al., 2005; Woo et al., 2004; Dou et al., 2012), electromagnetic wave absorption (Guo et al., 2017), but also as hot intelligent sensing (Alippi, 2016; Jin et al., 2016). The application of nanomaterials in the mentioned fields can be facilitated after modification of superparamagnetic nanoparticles with additional functional shells (organic or inorganic). Enrichment of the morphology of nanoparticles by introducing additional layers changes their primary properties and allows their potential applications to expand (Brollo et al., 2016; Amara et al., 2009). Thus, more than one characteristic of the core–shell structure can be used or it can be utilized in more effective way. A very important point in the preparation of the core–shell and multilayered nanoparticles is the quality of the interfacial region, which forms between chemically different

---

* Corresponding author.
E-mail address: kalska@uwb.edu.pl (B. Kalska-Szostko).

Peer review under responsibility of King Saud University.

Production and hosting by Elsevier

https://doi.org/10.1016/j.arabjc.2017.11.002
1878-5352

layers during the preparation of core–shell or multilayered nanoparticles (Giersig and Hilgendorff, 2005). In many cases, the degree of roughness of the interfacial region determines the physicochemical properties of the nanostructures due to the fact that it involves a large percentage of the total number of atoms when nanoparticles are combined (Andreeva et al., 2007; Aksenov, 2003). On the other hand, surface modification with chemically active metallic layers, for example, noble elements such as Ag, Au, and Cu, distinguishes new types of functionalization (Lu et al., 2010; Vékás et al., 2006; Sanvicens and Marco, 2008). Layers of noble metals also increase the number of substances that are possible to combine with magnetic nanoparticles. Therefore bioactive third particles (enzymes, DNA, and drugs) can be easily connected to them via adequate linkers (Das et al., 2008).

There are many surfactants (oleic acid (Haracz et al., 2015), ethyl oleate (Zheng et al., 2017), tetrabutylammonium hydroxide (Klekotka et al., 2017), many polymers (Sun et al., 2017) that efficiently covers magnetic core and prevents it from agglomeration, or oxidation or adds unique functionality. However, one should remember, that application of very complicated surface coating can influence the properties of the primary magnetic core. Our desire in this paper is to obtain nanoparticles with various metallic layers which change core characteristic, but not utilize very complicated organic coatings. It has to just prevent from the agglomeration. When properties of the inorganic core will be well controlled, the usage of more sophisticated (Zhang et al., 2017a) surface covering can be adopted (Zhang et al., 2017b; Yang et al., 2017).

In these studies, we analyze the influence of the nonmagnetic Ag, Au and Cu layers on the properties of a ferrite core and therefore the whole nanoparticle. Particles are prepared in one pot synthesis procedure. In our previous papers (Kalska-Szostko et al., 2013a; Kalska-Szostko et al., 2013b), we have observed that the nonmagnetic shell significantly changes the magnetic properties of the core. Because of that result, our current further studies include analyses of similar core–shell nanoparticles but prepared with modified fabrication methods, which control better subsequent growth and therefore changes of resultant properties. Due to lack of information in the literature about the ferrite multilayered nanoparticles, whereas an interlayer metal is used. Following studies focus on this subject and compare properties of particles which were fabricated in another manner. Proposed fabrication procedure minimizes any discrepancy between samples which are of randomization origin. These studies have been performed to understand the influence of the preparation procedures on the final properties of nanoparticles.

The aim of this investigation is to see how physicochemical properties change with nanoparticles core size, as well as the positioning of metallic/iron oxide layer inside particles. The positioning of the noble metal layer as middle or outermost can give information about the role of nonmagnetic material and its influence on magnetic properties of the core. Here also, chosen synthetic procedures reduce as much as possible the influence of inequivalent seeds.

2. Experimental

2.1. Material and apparatus

For the preparation of core–shell nanoparticles with various shells $Fe(acac)_3$, $Cu(acac)_2$, Gold (III) chloride 1,2-hexadecanediol and phenyl ether from Aldrich; $AgNO_3$ and oleic acid from POCH and additional 1-octadecanol and oleyl amine from Fluka were used. Cleaning and separation of the nanoparticles were performed with the use of acetone, sonication bath, and a permanent magnet.

Magnetic cores and layers were prepared from $Fe(acac)_3$ complexes. Non-magnetic metallic shells were obtained from proper precursors of Cu, Au, and Ag ions. All synthesized nanoparticles were measured to obtain structural characterization by X-ray diffraction (XRD) by Agilent Technologies SuperNova with a Mo microfocused source ($K_{\alpha 2} = 0.713067$ Å) diffractometer. The energy-dispersive X-ray spectroscopy (EDX) and transmission electron microscopy (TEM) measurements were done with a FEI Tecnai G2 X-TWIN 200 kV microscope to analyze composition morphology and crystallinity of the structure. Therefore the nanoparticles after dilution have been placed on a 400 mesh Cu grid. The short time temperature stability of the nanomaterials was tested by a Mettler Toledo Differential Scanning Calorimeter (DSC) with the STAR system. Infrared spectroscopy (IR) spectra were collected in the spectral range 500–4000 cm^{-1} with a Nicolet 6700 spectrometer working in reflecting mode. Mössbauer spectra were obtained with the use of the spectrometer working in constant acceleration mode with a $^{57}Co\underline{Cr}$ radioactive source. Metallic iron foil (α-Fe) was used as reference material. All samples were measured in transmission mode. Vibrating Sample Magnetometry measurements in the temperature range from 10 K to 300 K were performed on an MPMS SQUID and a PPMS vibrating sample magnetometer from Quantum Design.

2.2. Preparation of the core–shell magnetite nanoparticles

Magnetite seeds were obtained by vigorous mixing in the inert atmosphere (under continuous argon flow) of the following chemicals: $Fe(acac)_3$, 1,2-hexadecanediol, phenyl ether, oleylamine and oleic acid which had been mixed in one glass and heated to a temperature of around 259 °C for 30 minutes (Sun and Zeng, 2002; Kalska-Szostko et al., 2015). This procedure is well known in our team, therefore we decided to apply such synthetic method to achieve magnetic nanoparticles with most predictable properties. This way, the influence of metallic layer can be easily observed. The pristine seed particles were used as substrates to fabricate shells, obtained from $Fe(acac)_3$, $Cu(acac)_2$, $AgNO_3$ and $HAuCl_4$ compounds, respectively (Kalska-Szostko et al., 2015).

The magnetite seeds are synthesized twice and afterward they are used under modified conditions to obtain different type of core–shell nanoparticles which have the same core structure composition. In the first case, when the solution with seeds had been cooled down, $Fe(acac)_3$, 1-octadecanol, oleylamine and oleic acid were added to the mixture and heated to a temperature of 259 °C for 30 min (Kalska-Szostko et al., 2011). The resultant solution was divided into four equal parts. One was dried in deoxygenated acetone, and the three remaining parts were used in the following synthesis. In one part, Cu $(acac)_3$, 1,2-hexadecanediol, phenyl ether were combined, and heated up to 105 °C (Subramanian et al., 2011). At this temperature, oleylamine and oleic acid were added, and the whole mixture was heated and kept at 200 °C for 30 min. The other was modified by the addition of phenyl ether and then heated to 85 °C. A solution obtained from gold hydrochloride, phenyl ether, and oleyl amine was maintained at this temperature for a hour (Robinson et al., 2010). In the last part, $AgNO_3$, 1,2-hexadecanediol, phenyl ether and oleyl amine were mixed for 15 min at RT, then for 2 h at 30 °C, and at the end for 30 min at 140 °C (Lu et al., 2010). A schematic presentation of the above-described modifications is drawn in Fig. 1.

In the second type of synthesis, the seeds were at first divided into three parts. Each batch was modified by the metallic shell as described above by the addition of the same kind of chemicals to obtain Cu, Au, or Ag shells on the Fe-oxide cores. In the next step, every solution was again divided into two parts. One of each was dried in deoxygenated acetone, yielding nanoparticles with one shell. To the other parts, 4 mmol of $Fe(acac)_3$ complex was added with necessary supporting substrates. After this final synthesis procedure, the particles were washed with deoxygenated acetone and dried in an evaporator until powder form was obtained. Every step of the described procedure is schematically illustrated in Fig. 2.

The two presented fabrication methods produce nanoparticles with controlled composition. The usage of the same seed batch prevents random deviations of the synthesis conditions. A description of the prepared core–shell nanoparticles is collected in Table 1. The availability of particles from all stages of the fabrication process allows observation of any changes of the physicochemical properties connected with the addition of each subsequent layer on the nanoparticles. This coherent fabrication method reduces the influence of the stochastic distribution of the particle properties as a consequence of the variation of their size.

3. Results and discussion

3.1. Transmission electron microscopy

The quality of the nano-powders was analyzed by transmission electron microscopy. Selected images of all types of the prepared nanoparticles are depicted in Fig. 3.

It can be seen from TEM images collected in Fig. 3 that the prepared nanoparticles have well-defined size and near spherical shape. In the first image, the seed nanoparticles (Fe_3O_4 (A)) are shown. They have regular spherical shape and a size of about 8 ± 1 nm. In the case of nanoparticles with an added Fe-oxide layer, the particles preserve a round, regular shape and have an average size of 11 ± 2 nm. In the case of the core–shell nanoparticles, where the second layer of noble metals was used, the nanoparticles have sizes in an average of 12 ± 2 nm. These particles also did not deviate much from a regular spherical shape. The multilayered nanoparticles, where the last layer is a non-magnetic metallic layer, have sizes in the range of 12–15 with error bar 2 nm. In the type of nanoparticles where Cu, Au, and Ag serve as an interlayer between two magnetic (Fe-oxide) layers well-defined nanoparticles are observed but without a distinguished layered structure.

3.2. Energy-dispersive X-ray spectroscopy

The core–shell and multilayered nanoparticles were measured by EDX to control the composition of separate particles. In case of Fe_3O_4/Me and Fe_3O_4/Fe-ox/Me, adequate element specific signals in EDX spectra were obtained. Such results confirm the layered structure of the nanoparticles. Typical examples of the results are depicted in Fig. 4, where the insets present particle section.

The area element analyses confirm the presence of the requested metals in the particles. Element-specific line scans show the distribution of each metal in the whole particle and are in good agreement with the scenario of core–shell nanoparticles growth. The obtained values of the estimated percentage contribution of the different elements based on EDX analysis are collected in Table 2.

The tested values collected in Table 2 correlate well with the expected composition of the nanoparticles and the core–shell growth scenario. EDS number were summarized with XRD data. However, it should be undertaken that XRD gives not

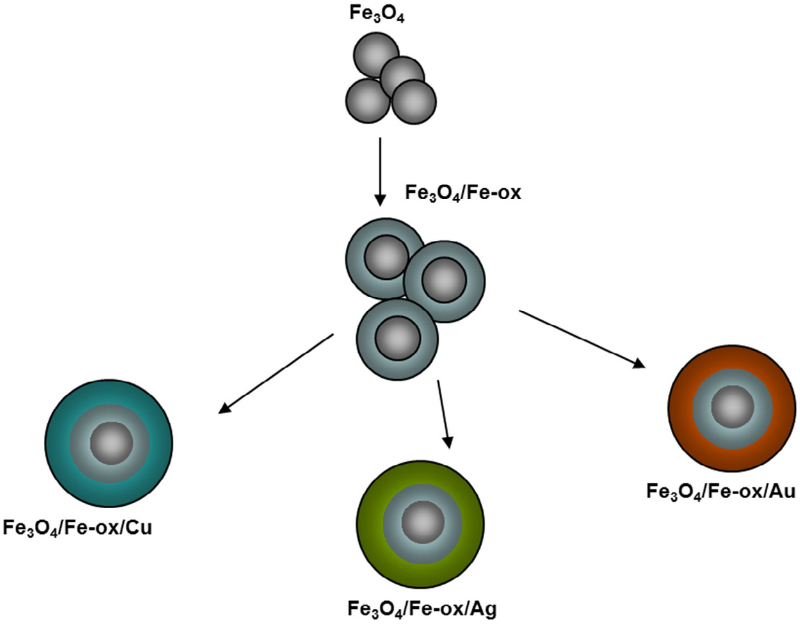

Fig. 1 Schematic illustration of the fabrication procedure of nanoparticles with various outermost metallic layers. Fe-ox stands for iron oxide (magnetite or maghemite).

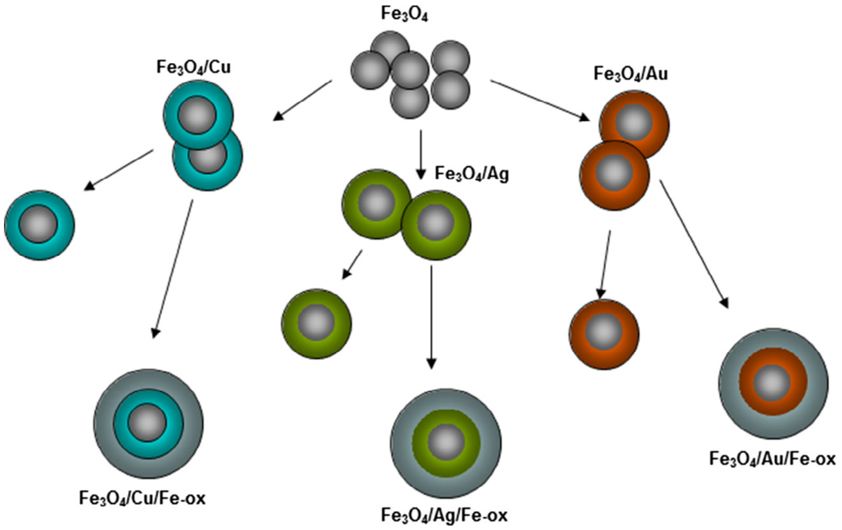

Fig. 2 Schematic illustration of the fabrication process of the multilayered nanoparticles with various spacing layers.

Table 1 Collection of core–shell nanoparticles. A schematic description of the nanoparticles is used; for example, Fe_3O_4/Fe-ox/Me means that nanoparticle has a ferrite core, then an iron oxide interlayer and finally a metallic shell (where Me varies between Ag, Au or Cu). The symbols (A) and (B) denote cores prepared using 4 or 6 mmol of $Fe(acac)_3$, respectively. Fe-ox states for iron oxide stand for magnetite or maghemite.

Nanoparticles	Core [mmol]	1st shell [mmol]	2nd shell [mmol]	Nanoparticles	Core [mmol]	1st shell [mmol]	2nd shell [mmol]
Fe_3O_4 (A)	4	–	–	Fe_3O_4 (B)	6	–	–
Fe_3O_4/Cu(A)	4	3	–	Fe_3O_4/Cu(B)	6	3	–
Fe_3O_4/Au(A)	4	0.44	–	Fe_3O_4/Au(B)	6	0.44	–
Fe_3O_4/Ag(A)	4	2	–	Fe_3O_4/Ag(B)	6	2	–
Fe_3O_4/Cu/Fe-ox(A)	4	3	4	Fe_3O_4/Cu/Fe-ox(B)	6	3	4
Fe_3O_4/Au/Fe-ox(A)	4	0.44	4	Fe_3O_4/Au/Fe-ox(B)	6	0.44	4
Fe_3O_4/Ag/Fe-ox(A)	4	2	4	Fe_3O_4/Ag/Fe-ox(B)	6	2	4
Fe_3O_4/Fe-ox(A)	4	4	–	Fe_3O_4/Fe-ox(B)	6	4	–
Fe_3O_4/Fe-ox/Cu(A)	4	4	3	Fe_3O_4/Fe-ox/Cu(B)	6	4	3
Fe_3O_4/Fe-ox/Au(A)	4	4	0.44	Fe_3O_4/Fe-ox/Au(B)	6	4	0.44
Fe_3O_4/Fe-ox/Ag(A)	4	4	2	Fe_3O_4/Fe-ox/Ag(B)	6	4	2

percentage of particular element, but crystal phase. Therefore, values will be not the same. The estimation of the elemental content from XRD underestimates the percentage of the metallic layer. This is partly due to the fact that detection of a crystalline phase is possible only when more than 5% of the whole volume possesses this structure. Also, the only crystalline phase is detected in XRD (e.g. diffusive scattering and amorphous phases are not counted) while each atom contributes to EDX analysis.

3.3. X-ray diffraction

Analyses of the crystal structure of the core–shell and layered nanoparticles were done by X-ray diffraction. The resulting diffractograms are depicted in series in Fig. 5. In Fig. 5A, diffractograms for two and three-layered nanoparticles are collected, where Ag, Au or Cu constitute the second layer and serve as interlayer or surface. In Fig. 5B, the diffractograms were collected for multilayered nanoparticles with Cu, Au, and Ag in the outermost layer, respectively. The reference magnetite patterns with indicated (i j k) Miller indices are shown together with the studied samples (Kalska-Szostko et al., 2014a; Mahadevan et al., 2007). The appearance of additional peaks in the diffractograms is a result of the presence of a crystalline metallic surface or interlayer.

It can be seen that changes in the seeds size result in changes of the relative ratio between the intensity of the signals from the magnetite and the noble metal layers. Each set of diffraction patterns shows well-defined signals of crystalline magnetite and patterns typically observed from Cu, Au and Ag metallic layers. These signals can be ascribed to the (1 1 1) (2 0 0) (2 2 0) (3 1 1) planes (Sinha and Sharma, 2005; Zhang et al., 1996) of the Cu, Au or Ag fcc lattices, but the cell parameters are different and therefore the reflections for the same (i j k) Miller indices do not appear at the same 2theta values for Cu, Ag or Au (a_{Ag} = 4.085 Å, a_{Au} = 4.0786 Å, and a_{Cu} = 3.6149 Å (Batchelder and Simmons, 1965; Novgorodova et al., 1981).

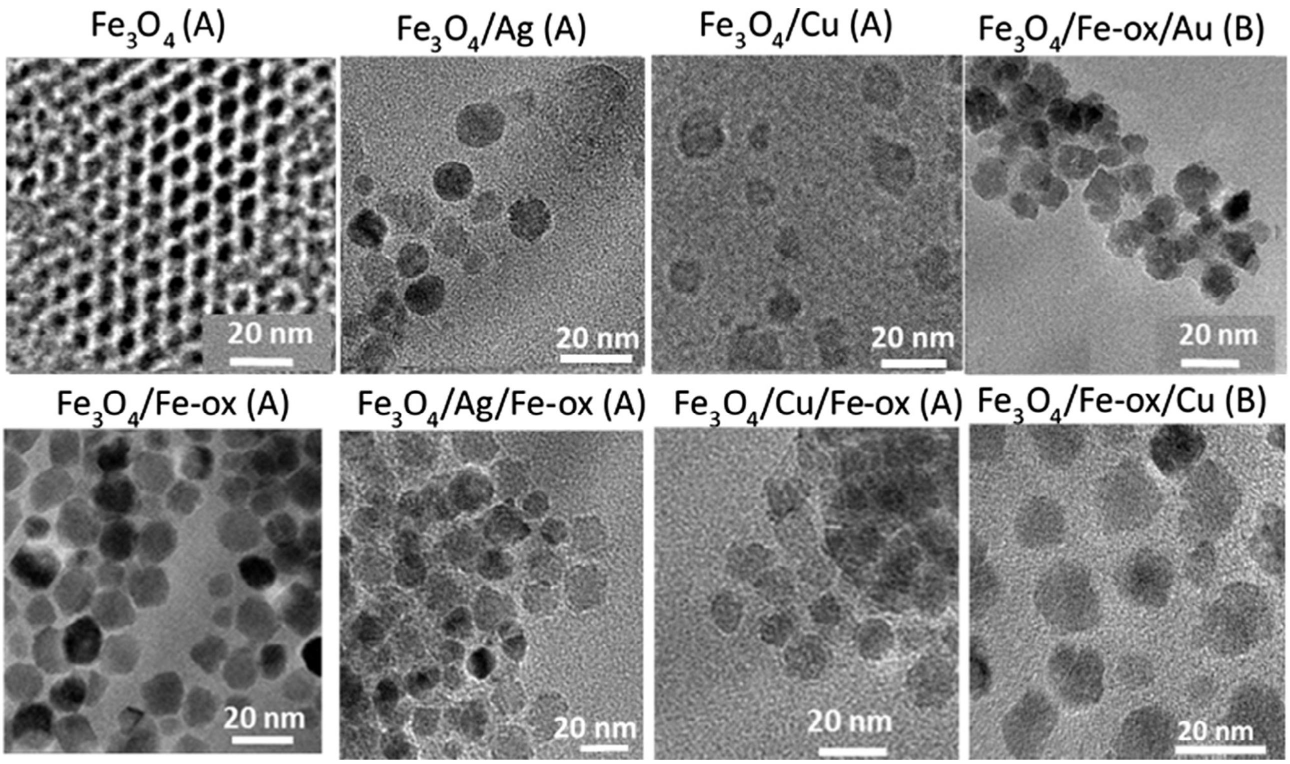

Fig. 3 TEM images of obtained seeds, core–shell, and multilayered nanoparticles.

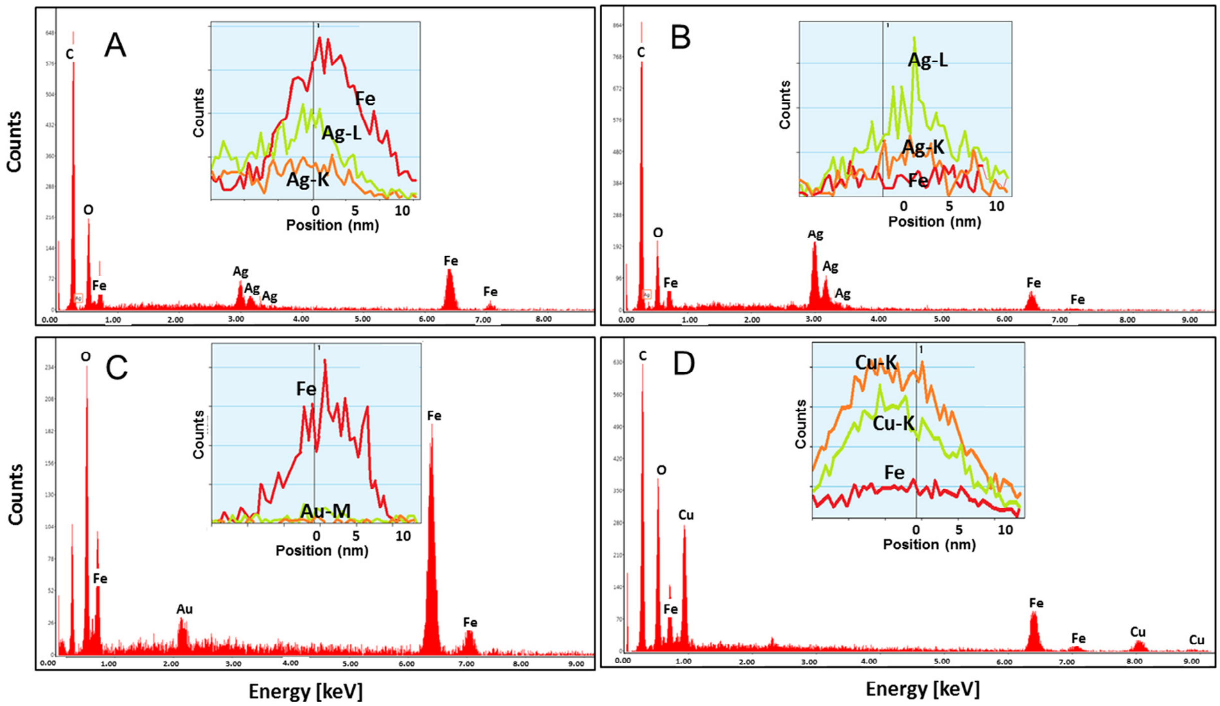

Fig. 4 Selected EDX results of some core–shell and multilayered nanoparticles with Fe(acac)$_3$ seeds. (A) Fe_3O_4/Ag/Fe-ox (A); (B) Fe_3O_4/Ag (B); (C) Fe_3O_4/Fe-ox/Au (A); (D) Fe_3O_4/Fe-ox/Cu (A).

Table 2 Percentage composition of oxide and metallic layer estimated from the EDX and XRD measurements. Only the content of Fe and Me is given.

Nanoparticles	Fe	Fe_3O_4	Me	Me-phase	Nanoparticles	Fe	Fe_3O_4	Me	Me-phase
	EDX ± 2 [%]	XRD	EDX ± 2 [%]	XRD		EDX ± 2 [%]	XRD	EDX ± 2 [%]	XRD
Fe_3O_4/Cu(A)	82	84	18	16	Fe_3O_4/Cu(B)	58	89	42	11
Fe_3O_4/Au(A)	96	93	4	7	Fe_3O_4/Au(B)	98	98	2	2
Fe_3O_4/Ag(A)	61	79	39	21	Fe_3O_4/Ag(B)	41	71	59	29
Fe_3O_4/Cu/Fe-ox(A)	80	90	20	10	Fe_3O_4/Cu/Fe-ox(B)	76	91	24	9
Fe_3O_4/Au/Fe-ox(A)	99	99	1	1	Fe_3O_4/Au/Fe-ox(B)	99	99	1	1
Fe_3O_4/Ag/Fe-ox(A)	80	79	20	21	Fe_3O_4/Ag/Fe-ox(B)	62	89	38	11
Fe_3O_4/Fe-ox/Cu(A)	46	64	61	36	Fe_3O_4/Fe-ox/Cu(B)	56	77	44	23
Fe_3O_4/Fe-ox/Au(A)	88	98	12	2	Fe_3O_4/Fe-ox/Au(B)	96	99	4	1
Fe_3O_4/Fe-ox/Ag(A)	43	83	57	17	Fe_3O_4/Fe-ox/Ag(B)	48	82	52	18

Moreover, the obtained X-ray results serve as a base for determination of the average grain size of the core–shell nanoparticles. Quantitative analyses were performed with Scherrer's Eq. (1) (Ghandoor et al., 2012) and the obtained diameters are summarized in Table 2.

$$D = \frac{0.9 \cdot \lambda}{\beta \cdot \cos \theta} \tag{1}$$

where D – grain size [Å], λ – wavelength (for Mo source is 0.7136 Å), β – full width at half maximum intensity of the peak [rad], and θ – diffraction angle [rad].

In our analysis, we used (3 1 1) reflection of the magnetite signal.

From the XRD line position in the 2theta range also the widening originating from the strain of the structure can be estimated according to the Williamson-Hall law using the following equation (Zak et al., 2011):

$$\beta \cos \theta = \left(\frac{0.9\lambda}{D} \right) + (4\varepsilon \sin \theta) \tag{2}$$

where ε is a strain of the structure.

The parameters extracted from the diffractograms including lattice parameters, particle size and strain are presented in Table 3. The XRD radius is calculated from the magnetite peaks, thus excluding the surface or interface metallic layer. The lattice constants were extracted for both phases.

According to the changes of the calculated values of the average particle size, the idea of layered growth can be followed. Obtained values from XRD data show not only growth of the grain size with the increase of Fe precursor but also clearly indicate the influence of metallic layer on the lattice constant of magnetite which is always, in case of Ag, most disturbed in comparison to bulk magnetite value (8.39 Å) (Blaney, 2007). This is in good agreement with the prediction of the core–shell particles fabrication and subsequent layered growth. The presented grain size is taken from magnetite patterns, therefore total particles volume can be different (metallic layer was not taken into account). The lattice constant of metallic layer calculated from XRD is also in good agreement with bulk values of respective metals. The increase of the strain value measured on magnetite reflects the influence upon the additional structurally different layer or crystallinity of magnetite. It is observed that in any case, the presence of the Me layer at the surface causes less stress than interlayer. The seed nanoparticles have a calculated average grain size around 7 or 9 ± 1 nm, and an addition of any next layer causes an increase of the measured diameter. The multilayered nanoparticles have a bigger grain size in comparison to the respective core–shell structure. Observed discrepancy between imaged by TEM particles size and these obtained from XRD is originated in the difference in sampling and data estimation. XRD is an average parameter over a large number of particles, and size refers only to ferrite part. Averaging is done from TEM over a relatively low particles number ($\sim$100), and regardless of the layer composition, morphology is the same. Therefore obtained data can be different. Besides that, XRD to the line width has significant input on other effects presented in the system: structure stress, crystalline disorder, dislocations, size and chemical distributions, apparatus properties, etc. Presented values in Table 4, however, do not disagree with each other. Therefore, XRD data can be treated as estimation or reference data only, not as real values.

3.4. Differential Scanning Calorimetry

A thermal analysis of magnetite seeds and core–shell nanoparticles with Au, Ag or Cu shells with quick heating and cooling cycle in temperature range 20–450 °C with a scan rate of 10 °C/min was performed. As a reference, an empty pan was used. For DSC measurement, a quantity of roughly 2 mg of the total weight of the sample was separated. Obtained thermal curves are depicted in Fig. 6.

The DSC curve of the seed nanoparticles does not show any thermal changes in the investigated temperature range. The core–shell nanoparticles with Au shell show a wide endothermic process from 126 to 226 °C with a heat content of −918 mJ and a weak exothermic process at 240–308 °C. In the nanoparticles with the Cu layer, an endothermic process at 103–176 °C and a weak exothermic peak at 327–367 °C are seen. The nanoparticles with an Ag shell exhibit a wide endothermic process at temperatures 138–213 °C with a heat content of -318 mJ and an intensive endothermic change at 277–259 °C containing −2307 mJ of heat. The results show that the addition of noble metal layers causes thermal activity of the samples in the temperature range 20–450 °C of different magnitude and that the addition of Cu shells changes thermal stability of the core in the gentlest way.

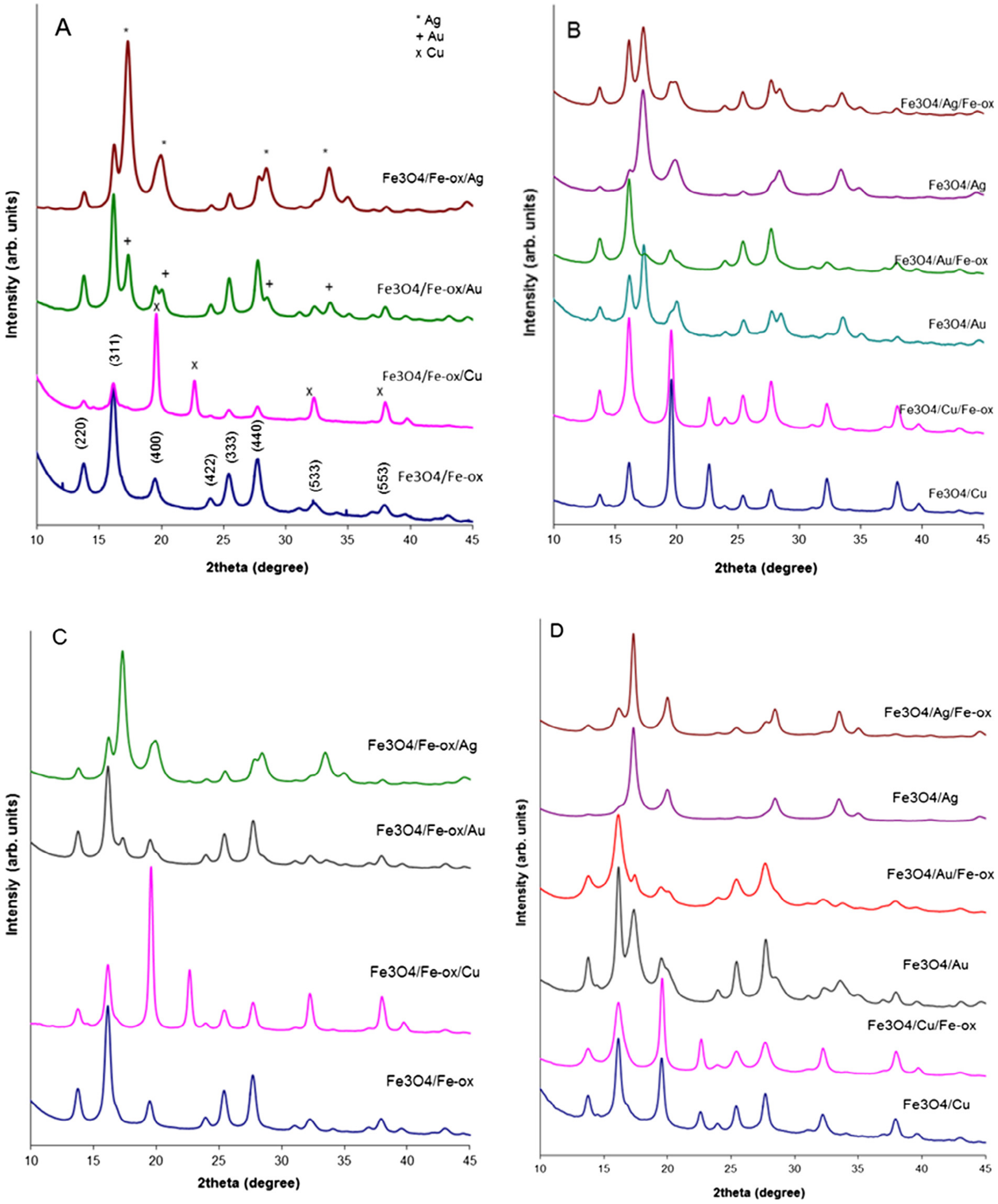

Fig. 5 XRD patterns of core–shell nanoparticles with respective shells. In A and B panels nanoparticles with 4 mmol core are collected, in C and D- with 6 mmol core, respectively.

3.5. IR spectroscopy

For IR analyses, a small amount of each powder was deposited on a diamond window and the spectra were measured in reflection mode. The IR spectra should reveal surface modifications after different synthesis procedures.

Representative IR spectra of multilayered nanoparticles with various outermost layers prepared from Ag, Au, Cu or Fe-ox are depicted in Fig. 7. Every spectrum shows typical signals for Fe—O bonds originating from magnetite (570 cm^{-1}) (Namduri and Nasrazadani, 2008; Kalska-Szostko et al., 2014b). There are also signals from bonds of organic

Table.3 Estimated grain sizes, lattice constants and strains of core–shell nanoparticles determined by X-ray diffraction.

Nanoparticles	Grain size ± 2 [nm]	Lattice constant [Å] ± 0.02		Strain ± 0.5 [10 $^{-3}$]	Nanoparticles	Grain size ± 2 [nm]	Lattice constant [Å] ± 0.02		Strain ± 0.5 [1 0 $^{-3}$]
		Fe_3O_4	Me				Fe_3O_4	Me	
Fe_3O_4 (A)	9	8.37	–	6.7	Fe_3O_4 (B)	7	8.36	–	5.6
Fe_3O_4/Cu(A)	11	8.39	3.64	3.5	Fe_3O_4/Cu(B)	5	8.49	3.97	1.6
Fe_3O_4/Au(A)	10	8.38	4.08	4.4	Fe_3O_4/Au(B)	10	8.36	4.07	3.5
Fe_3O_4/Ag(A)	11	8.40	4.10	3.0	Fe_3O_4/Ag(B)	8	8.49	4.14	0.5
Fe_3O_4/Cu/Fe-ox(A)	12	8.38	3.61	5.1	Fe_3O_4/Cu/Fe-ox(B)	8	8.49	3.70	4.7
Fe_3O_4/Au/Fe-ox(A)	10	8.38	4.04	5.5	Fe_3O_4/Au/Fe-ox(B)	12	8.38	4.04	9.3
Fe_3O_4/Ag/Fe-ox(A)	11	8.40	4.09	4.6	Fe_3O_4/Ag/Fe-ox(B)	10	8.46	4.10	3.1
Fe_3O_4/Fe-ox(A)	11	8.36	–	4.1	Fe_3O_4/Fe-ox(B)	12	8.37	–	4.9
Fe_3O_4/Fe-ox/Cu(A)	13	8.38	3.61	4.8	Fe_3O_4/Fe-ox/Cu(B)	13	8.38	3.61	4.0
Fe_3O_4/Fe-ox/Au(A)	13	8.38	4.07	4.3	Fe_3O_4/Fe-ox/Au(B)	12	8.38	4.07	3.3
Fe_3O_4/Fe-ox/Ag(A)	14	8.39	4.10	5.5	Fe_3O_4/Fe-ox/Ag(B)	13	8.39	4.10	3.4

Table 4 Magnetization values calculated from hysteresis curves. M_{rs} – saturation remanence, M_s – saturation magnetization; H_c – coercive field; χ_{hf}- high-field susceptibility.

Temperature [K]	M_{rs} [mA·m^2/kg]	M_s [mA·m^2/kg]	H_c [mT]
2	7.3	26.1	14.4
10	4.6	25.2	8.7
300	1.8	20.3	4.4

compounds used during synthesis. The signals marked at 720 cm^{-1} and 2920–2851 cm^{-1} belong to C—C bonds in carbon chains from oleic acid. The very characteristic band at 1404–1564 cm^{-1} is due to the presence of acetylacetonate salt groups (Coates, 2000), and the one at 3325 cm^{-1} is obtained from —OH bonds in water adsorbed from the air. The spectrum of Fe_3O_4/Fe-ox/Ag nanoparticles (Fig. 7A) shows, in addition, a weak signal around 630 cm^{-1} which reflects oxidation of magnetite to maghemite (Kalska-Szostko et al., 2013c). The weak band at 2348 cm^{-1} is observed due to a high amount of —NH_2 group present on the surface of the nanoparticles. The spectra of Fe_3O_4/Fe-ox/Ag and Fe_3O_4/Fe-ox/Cu nanoparticles have additional signals at 1017–1050 cm^{-1} indicating oxidation of the nanoparticles surface from magnetite to lepidocrocite (Kalska-Szostko et al., 2013c; Balasubramaniam and Ramesh Kumar, 2000). Signals present at 1238 cm^{-1} (observed in the spectrum C) are typical for Ar—O—Ar bonds from diphenyl ether and bond at 1738 cm^{-1} can be caused by C═O bonds which are left after synthesis procedure.

3.6. Magnetometry

Magnetic properties of selected samples were measured in the temperature range from 10 K to room temperature. Low field (50 Oe) magnetization vs. temperature measurements using zero fields cooled (ZFC) and field cooled (FC) protocols were performed. Resulting curves are plotted in Fig. 8, together with superparamagnetic blocking temperatures estimated from the formula given by Hansen and Mørup (Hansen and Mørup, 1999).

Panel A shows M vs. T curves for samples (from the preparation process A) covered with Cu layers. The blocking temperature of these samples is to be found above 300 K. In panel B three curves are collected (again from the preparation process A) where the top is Fe_3O_4/Fe-ox, middle has Cu capping and the bottom one Ag as a surface layer. The derived blocking temperatures are indicated in the panels and are 200, 170 and 75 K, respectively. The blocking temperature decreases with the addition of a metallic capping layer, slightly for a Cu layer and more significantly with an Ag layer. A corresponding decrease of the blocking temperature with an added Cu (140–80 K) shell is derived from the two panels in C where the core seed is from the preparation process B.

In Fig. 9 example of hysteresis curves collected at 2 K, 10 K, and 300 K are depicted. The inset presents magnification of center part of the plot to see very small values of the coercive field which increases up to the max. 14.4 mT at 300 K. For particles with core–shell morphology and presence of noble metal saturation magnetization per gram decreases significantly what is clearly connected with the presence of nonmagnetic layer.

3.7. Mössbauer spectroscopy

Selected Mössbauer spectra of core–shell and multilayered nanoparticles are collected in Fig. 10.

The RT Mössbauer spectra are shown in such a way that particles fabricated from the same seeds are in one panel. Therefore the evolution of the spectra with the added layers should be compared inside one figure. In panel (A) spectra of particles fabricated on 6 mmol seeds are depicted. It is seen that addition of the noble metal and on top of this, an extra Fe-oxide layer causes modification of Mössbauer spectra in such a way that the superparamagnetic singlet/doublet (Zhu et al., 2011) decreases and a wide sextet appear. This is in agreement with the scenario of layered growth of the particles. The spectra of all samples with added metal layers have a wider background signal, which suggests an increase of the superparamagnetic blocking temperature. It can also suggest improvement of cross-talking between layers inside a single particle or/and changes of the interfacial region so that the

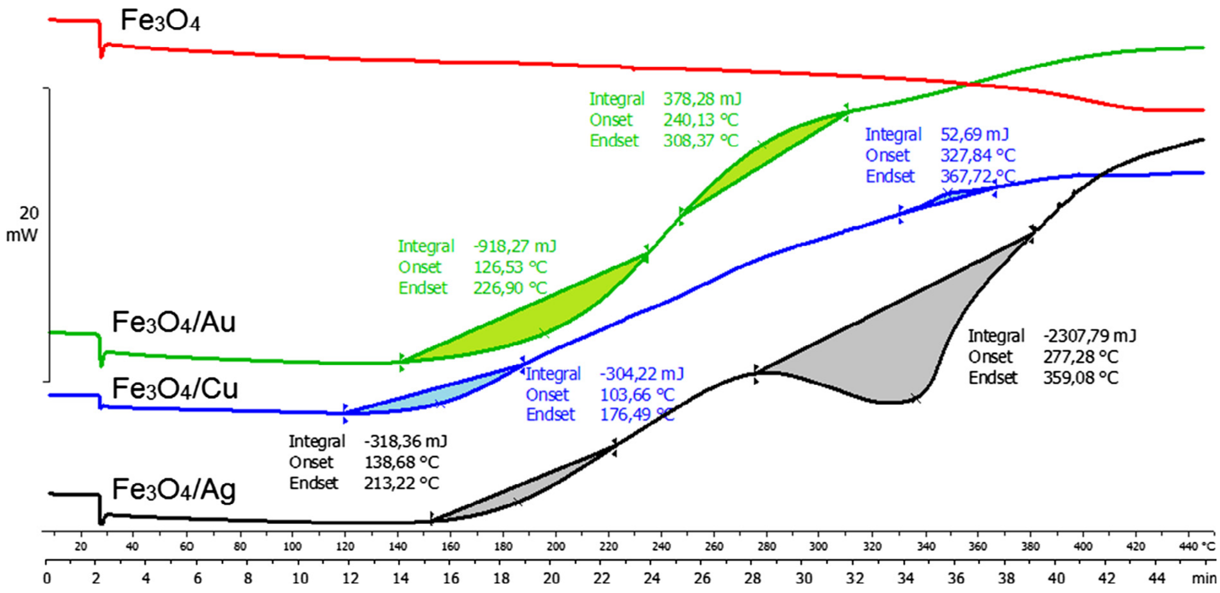

Fig. 6 DSC curves of magnetic seeds and core–shell nanoparticles.

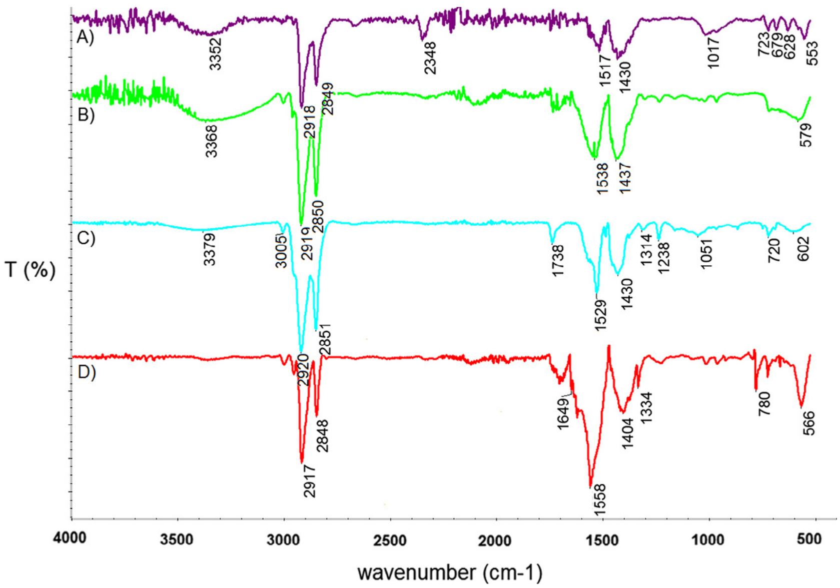

Fig. 7 IR spectra of multilayered nanoparticles (A) Fe_3O_4/Fe-ox/Ag(A); (B) Fe_3O_4/Fe-ox/Au(A); (C) Fe_3O_4/Fe-ox /Cu(A); (D) Fe_3O_4/Fe-ox (A).

average magnetic moment is frozen at the certain direction and superparamagnetic fluctuation is suppressed. The interaction between particles is also a possible reason for splitting. The most pronounced widening of the spectra is for the Cu covered particles. Panel B shows spectra for particles where a third metal layer was added. Careful examination of the spectra indicates an increase of the blocking temperature when metal layers are added. A continuous modification of the spectra is seen and it is only a result of the addition of chemically different surface layers. Panel C shows spectra from samples where the size of the magnetic core supposed to be is enlarged by an increase of the precursor amount in the seeds synthesis. There, the second metallic layer was added and on the top – Fe-oxide, similar to the samples in panel (A). As it is seen, the surface layers modify the MS spectra; in this case, each of them is split into distinct sextets. This suggests interaction (cross-talking) between the Fe layers inside particles via the metallic spacing layer.

In general, in each case, the presence of a Cu layer causes the most split spectra. This observation is valid for each studied series of nanoparticle samples. From Mössbauer spectra modulation in the series, it can be concluded that the origin of splitting arises from enhanced superparamagnetic blocking temperatures of the samples. Surprisingly, the estimated blocking temperatures based on the ZFC/FC magnetization curves suggest opposite phenomena to the one obtained from MS data. This is surprising in spite of the very different observation time characteristic of Mössbauer spectroscopy (10–7 s)

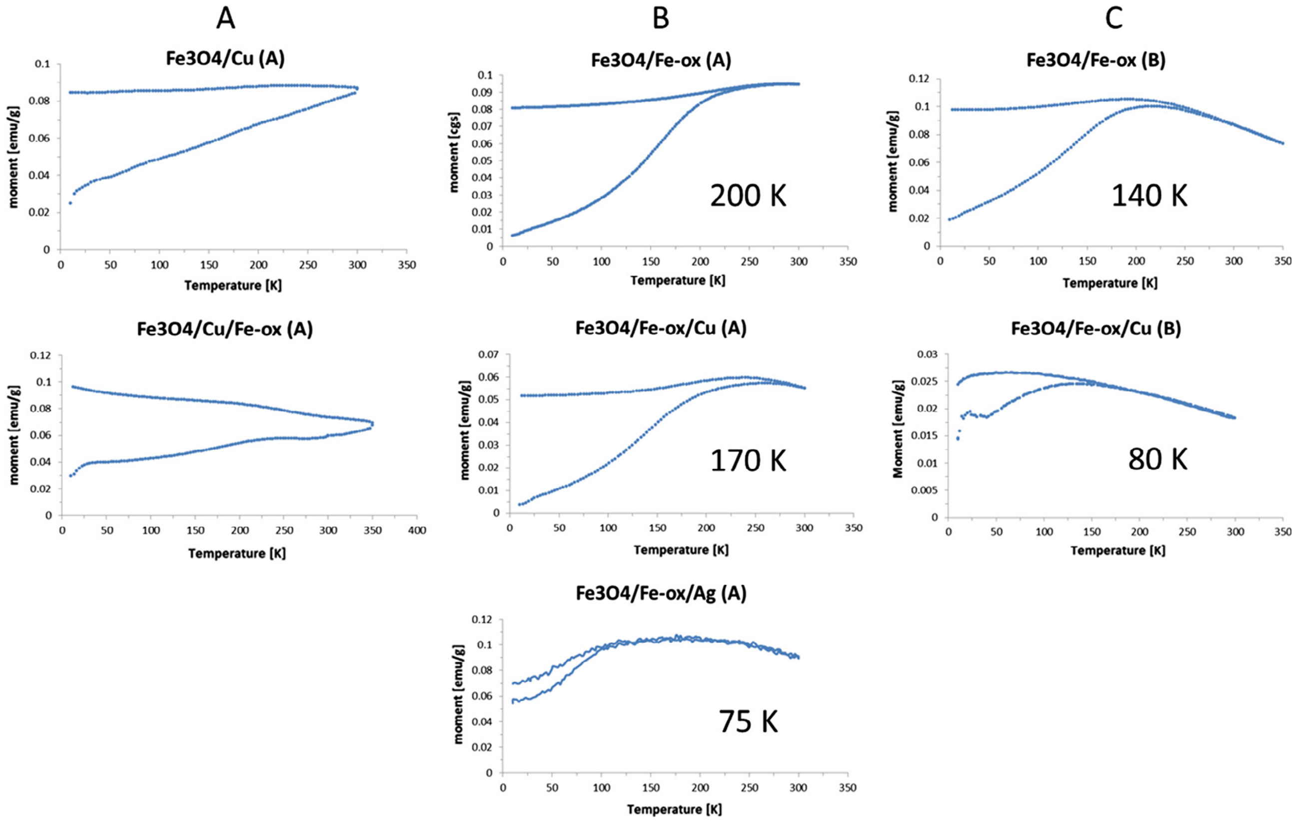

Fig. 8 ZFC/FC magnetization vs. temperature curves for selected core–shell and multilayered nanoparticles.

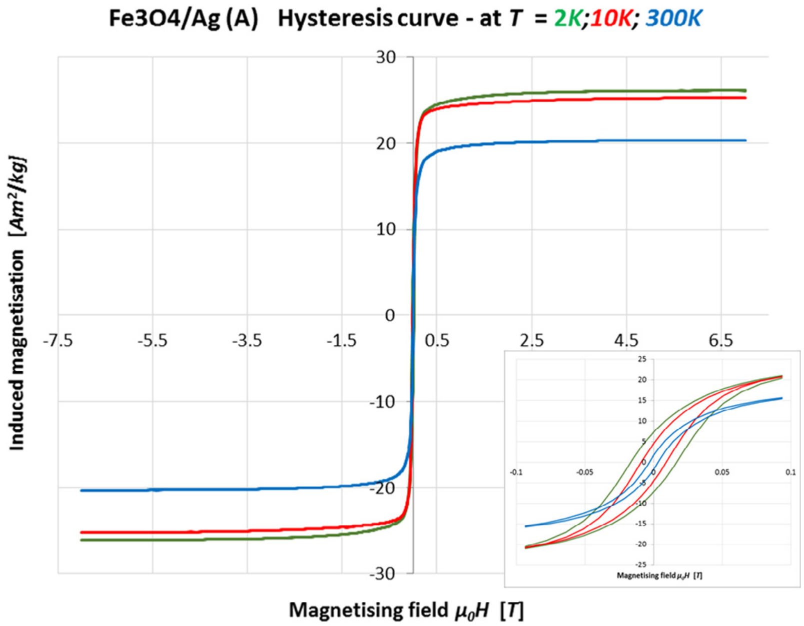

Fig. 9 Hysteresis curves of Fe_3O_4/Ag (A) nanoparticles, at temperatures 2 (green), 10 (red), and 300 K (blue), respectively.

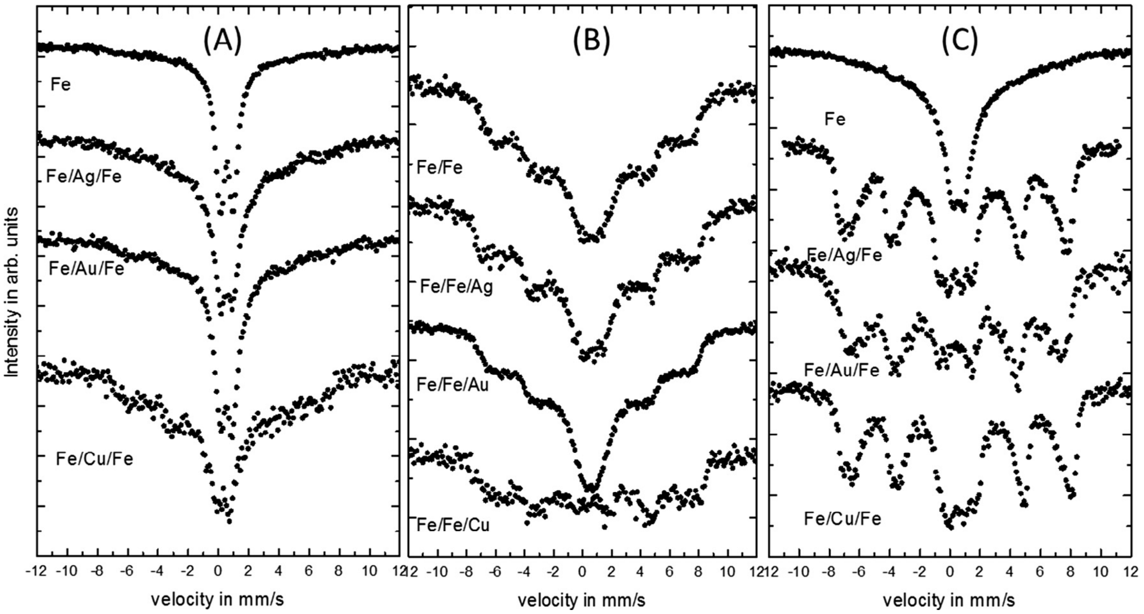

Fig. 10 Mössbauer spectra of core–shell nanoparticles from tree series.

and magnetization experiments (100 s). However, such discrepancy supports the thesis that it has been another mechanism involved in growth (Yin and Alivisatos, 2005).

4. Conclusion

This paper presents continuation and expansion of studies on preparation of core–shell nanoparticles where magnetic core and metallic layers were obtained by layer-by-layer growth method. It is shown, that with this fabrication model various thickness of metallic and oxide shells can be obtained. Presented TEM images show that with the addition of any layer (metallic or iron oxide), their size increases, and additional EDX measurements profs presence of added layers. The Mössbauer spectra of the magnetite nanoparticles seed particles change after each subsequent layer addition and they were monitored in a step-by-step manner. The influence of the added metal and Fe-oxide layers on the Mössbauer spectra are discussed. Magnetization measurements reveal the opposite trend of the blocking temperatures as compared to that derived from Mössbauer spectra. XRD patterns prove a chemically modulated structure of the obtained particles. Presented fabrication procedure eliminates the environmental parameters random influence on final particles.

Acknowledgement

Mössbauer spectroscopy was done in close collaboration with Department of Physics of the University of Bialystok. Authors thank for dr Simo Spassov for hysteresis curve measurements. The VSM measurements were performed during the COST Short-Therm Scientific Mission number COST-MP1302. The work was partially financed by EU funds via the projects with a contract number POPW.01.03.00-20-034/09-00, POPW. 01.03.00-20-004/11-00 and by NCS-Poland funds, project number 2014/13/N/ST5/00568.

References

Ahadpour Shal, A., Jafari, A., 2014. Study of Structural and magnetic properties of superparamagnetic Fe_3O_4–ZnO core–shell nanoparticles. J. Supercond. Nov. Magn. 27, 1531–1538.

Aksenov, V.L. et al, 2003. Polarized neutron reflectometry studies of depth magnetization distribution in Fe/V layered structure. J. Magn. Magn. Mater. 258, 332–334.

Alippi, C., 2016. A unique timely moment for embedding intelligence in applications. CAAI Trans. Intell. Technol. 1, 1–3.

Amara, D., Felner, I., Nowik, I., Margel, S., 2009. Synthesis and characterization of Fe and Fe_3O_4 nanoparticles by thermal decomposition of triiron dodecacarbonyl. Colloids Surfaces A Physicochem. Eng. Asp. 339, 106–110.

Andreeva, M.A., Monina, N.G., Lindgren, B., Häggström, L., Kalska, B., 2007. Magnetic ordering in a [Fe/Co]35 BCC film studied by nuclear resonant reflectometry. J. Exp. Theor. Phys. 104, 577–585.

Angelakeris, M. et al, 2015. Enhanced biomedical heat-triggered carriers via nanomagnetism tuning in ferrite-based nanoparticles. J. Magn. Magn. Mater. 381, 179–187.

Balasubramaniam, R., Ramesh Kumar, A.V., 2000. Characterization of Delhi iron pillar rust by X-ray diffraction, Fourier transform infrared spectroscopy and Mossbauer spectroscopy. Corros. Sci. 42, 2085–2101.

Batchelder, D.N., Simmons, R.O., 1965. X ray lattice constants of crystals by a rotating camera method: Al, Ar, Au, CaF_2, Cu, Ge, Ne. Si. J. Appl. Phys. 36, 2864–2868.

Blaney, L., 2007. Magnetite (Fe3O4): properties, synthesis, and applications. The Lehigh Rev. 15, 5.

Brollo, M.E.F. et al, 2016. Magnetic hyperthermia in brick-like Ag@Fe_3O_4 core-shell nanoparticles. J. Magn. Magn. Mater. 397, 20–27.

Coates, J., 2000. Interpretation of infrared spectra, a practical approach. Encycl. Anal. Chem., 10815–10837 https://doi.org/10.1002/9780470027318.

Das, M., Mishra, D., Maiti, T.K., Basak, A., Pramanik, P., 2008. Bio-functionalization of magnetite nanoparticles using an aminophosphonic acid coupling agent: new, ultradispersed, iron-oxide folate nanoconjugates for cancer-specific targeting. Nanotechnology 19, 415101.

Dou, J., Zhang, Q., Ma, M., Gu, J., 2012. Fast fabrication of epoxy-functionalized magnetic polymer core-shell microspheres using glycidyl methacrylate as monomer via photo-initiated miniemulsion polymerization. J. Magn. Magn. Mater. 324, 3078–3082.

Ghandoor, H. El, Zidan, H.M., Khalil, M.M.H., Ismail, M.I.M., 2012. Synthesis and Some Physical Properties of Magnetite (Fe_3O_4) Nanoparticles. Int. J. Electrochem. Sci. 7, 5734–5745.

Giersig, M., Hilgendorff, M., 2005. Magnetic nanoparticle superstructures. Eur. J. Inorg. Chem. 3571–3583. https://doi.org/10.1002/ejic.200500497.

Guo, J. et al, 2017. Polypyrrole-interface-functionalized nano-magnetite epoxy nanocomposites as electromagnetic wave absorbers with enhanced flame retardancy. J. Mater. Chem. C 5, 5334–5344.

Hansen, M.F., Mørup, S., 1999. Estimation of blocking temperatures from ZFC/FC curves. J. Magn. Magn. Mater. 203, 214–216.

Haracz, S., Hilgendorff, M., Rybka, J.D., Giersig, M., 2015. Effect of surfactant for magnetic properties of iron oxide nanoparticles. Nucl. Instrum. Methods Phys. Res. Sect. B Beam Interact. Mater. Atoms 364, 120–126.

Jin, H., Chen, Q., Chen, Z., Hu, Y., Zhang, J., 2016. Multi-LeapMotion sensor based demonstration for robotic refine tabletop object manipulation task. CAAI Trans. Intell. Technol. 1, 104–113.

Kalska-Szostko, B., Cydzik, M., Satuła, D., Giersig, M., 2011. Mössbauer studies of core-shell nanoparticles. 119, 3–5.

Kalska-Szostko, B., Wykowska, U., Nordblad, P., Satula, D., 2015. Thermal treatment of magnetite nanoparticles. Beilstein J. Nanotechnol. 6, 1385.

Kalska-Szostko, B., Wykowska, U., Piekut, K., Zambrzycka, E., 2013c. Stability of iron (Fe) nanowires. Colloids Surfaces A Physicochem. Eng. Asp. 416, 66–72.

Kalska-Szostko, B., Wykowska, U., Basa, A., Szymański, K., 2013b. Chemical preparation of core-shell nanoparticles. Nukleonika 58, 35–38.

Kalska-Szostko, B., Rogowska, M., Satuła, D., 2013a. Organophosphorous functionalization of magnetite nanoparticles. Colloids Surfaces B Biointerfaces 111, 656–662.

Kalska-Szostko, B., Wykowska, U., Satuła, D., Zambrzycka, E., 2014a. Stability of core-shell magnetite nanoparticles. Colloids Surfaces B Biointerfaces 113, 295–301.

Kalska-Szostko, B., Wykowska, U., Piekut, K., Satuła, D., 2014b. Stability of Fe3O4 nanoparticles in various model solutions. Colloids Surfaces A Physicochem. Eng. Asp. 450, 15–24.

Kalska-Szostko, B., Wykowska, U., Satuła, D., 2015. Magnetic nanoparticles of core-shell structure. Colloids Surfaces A Physicochem. Eng. Asp. 481, 527–536.

Klekotka, U., Rogowska, M., Satuła, D., Kalska-Szostko, B., 2017. Characterization of ferrite nanoparticles for preparation of biocomposites. Beilstein J. Nanotechnol. 8, 1257–1265.

Lingyan Wang, L.W. et al., 2005. Monodispersed core–shell Fe3O4@Au nanoparticles. https://doi.org/10.1021/JP0543429.

Lu, L. et al, 2010. Fe@Ag core-shell nanoparticles with both sensitive plasmonic properties and tunable magnetism. Mater. Lett. 64, 1732–1734.

Mahadevan, S., Gnanaprakash, G., Philip, J., Rao, B.P.C., Jayakumar, T., 2007. X-ray diffraction-based characterization of magnetite nanoparticles in presence of goethite and correlation with magnetic properties. Phys. E Low-Dimen. Syst. Nanostruct. 39, 20–25.

Namduri, H., Nasrazadani, S., 2008. Quantitative analysis of iron oxides using Fourier transform infrared spectrophotometry. Corros. Sci. 50, 2493–2497.

Novgorodova, M.I., Gorshkov, A.I., Mokhov, A.V., 1981. Native silver and its new structural modifications. Int. Geol. Rev. 23, 485–494.

Robinson, I., Tung, L.D., Maenosono, S., Wälti, C., Thanh, N.T.K., 2010. Synthesis of core-shell gold coated magnetic nanoparticles and their interaction with thiolated DNA. Nanoscale 2, 2624–2630.

Sanvicens, N., Marco, M.P., 2008. Multifunctional nanoparticles – properties and prospects for their use in human medicine. Trends Biotechnol. 26, 425–433.

Sinha, A., Sharma, B.P., 2005. Preparation of silver powder through glycerol process. Bull. Mater. Sci. 28, 213–217.

Subramanian, N.D., Moreno, J., Spivey, J.J., Kumar, C.S.S.R., 2011. Copper core-porous manganese oxide shell nanoparticles. J. Phys. Chem. C 115, 14500–14506.

Sun, K. et al, 2017. Flexible polydimethylsiloxane/multi-walled carbon nanotubes membranous metacomposites with negative permittivity. Polym. (United Kingdom) 125, 50–57.

Sun, S.H., Zeng, H., 2002. Size-controlled synthesis of magnetite nanoparticles. J. Am. Chem. Soc. 124, 8204–8205.

Vatta, L.L., Sanderson, R.D., Koch, K.R., 2006. Magnetic nanoparticles: Properties and potential applications. Adv. Mater. 78, 1793–1801.

Vékás, L., Bica, D., Marinica, O., 2006. Magnetic nanofluids stabilized with various chain length surfactants. Rom. Reports Phys. 58, 257–267.

Woo, K., et al., 2004. Easy synthesis and magnetic properties of iron oxide nanoparticles. https://doi.org/10.1021/CM049552X.

Xiong, Z. et al, 2013. Layer-by-layer assembly of multilayer polysaccharide coated magnetic nanoparticles for the selective enrichment of glycopeptides. Chem. Commun. 49, 9284–9286.

Yang, W. et al, 2017. Polyoxymethylene/ethylene butylacrylate copolymer/ethylene-methyl acrylate-glycidyl methacrylate ternary blends. Polym. Eng. Sci. https://doi.org/10.1002/pen.24675.

Yin, Y., Alivisatos, A.P., 2005. Colloidal nanocrystal synthesis and the organic–inorganic interface. Nature 437, 664–670.

Zak, A.K., Majid, W.H.A., Abrishami, M.E., Yousefi, R., 2001. X-ray analysis of ZnO nanoparticles by Williamsone Hall and sizeestrain plot methods. https://doi.org/10.1016/j.solidstatesciences.2010.11.024.

Zhang, K. et al, 2017b. Ultralow percolation threshold and enhanced electromagnetic interference shielding in poly(l-lactide)/multi-walled carbon nanotube nanocomposites with electrically conductive segregated networks. J. Mater. Chem. C 5, 9359–9369.

Zhang, L. et al, 2017a. Large scaled synthesis of heterostructured electrospun TiO_2/SnO_2 nanofibers with an enhanced photocatalytic activity. J. Electrochem. Soc. 164, H651–H656.

Zhang, K., Alexandrov, I.V., Valiev, R.Z., Lu, K., 1996. Structural characterization of nanocrystalline copper by means of x ray diffraction. J. Appl. Phys. 80, 5617–5624.

Zheng, Y. et al, 2017. Esterification synthesis of ethyl oleate catalyzed by Brønsted acid–surfactant-combined ionic liquid. Green Chem. Lett. Rev. 10, 202–209.

Zhu, J. et al, 2011. Surfactant-free synthesized magnetic polypropylene nanocomposites: rheological, electrical, magnetic, and thermal properties. Macromolecules 44, 4382–4391.

Zhu, Y., Da, H., Yang, X., Hu, Y., 2003. Preparation and characterization of core-shell monodispersed magnetic silica microspheres. Colloids Surfaces A Physicochem. Eng. Asp. 231, 123–129.